

On the Structure of the Sagittarius Spiral Arm in the Inner Milky Way

S. B. BIAN,^{1,2} Y. W. WU,³ Y. XU,^{1,2} M. J. REID,⁴ J. J. LI,¹ B. ZHANG,⁵ K. M. MENTEN,⁶ L. MOSCADELLI,⁷ AND
A. BRUNTHALER⁶

¹*Purple Mountain Observatory, Chinese Academy of Sciences, Nanjing 210033, China; xuye@pmo.ac.cn*

²*School of Astronomy and Space Science, University of Science and Technology of China, Hefei 230026, China*

³*National Time Service Center, Key Laboratory of Precise Positioning and Timing Technology, Chinese Academy of Sciences, Xi'an 710600, China*

⁴*Center for Astrophysics | Harvard & Smithsonian, 60 Garden Street, Cambridge, MA 02138, USA*

⁵*Shanghai Astronomical Observatory, Chinese Academy of Sciences, Shanghai 200030, China*

⁶*Max-Planck-Institut für Radioastronomie, Auf dem Hügel 69, 53121 Bonn, Germany*

⁷*INAF-Osservatorio Astrofisico di Arcetri, Largo E. Fermi 5, 50125 Firenze, Italy*

ABSTRACT

We report measurements of trigonometric parallax and proper motion for two 6.7 GHz methanol and two 22 GHz water masers located in the far portion of the Sagittarius spiral arm as part of the BeSSeL Survey. Distances for these sources are estimated from parallax measurements combined with 3-dimensional kinematic distances. The distances of G033.64–00.22, G035.57–00.03, G041.15–00.20, and G043.89–00.78 are 9.9 ± 0.5 , 10.2 ± 0.6 , 7.6 ± 0.5 , and 7.5 ± 0.3 kpc, respectively. Based on these measurements, we suggest that the Sagittarius arm segment beyond about 8 kpc from the Sun in the first Galactic quadrant should be adjusted radially outward relative to previous models. This supports the suggestion of Xu et al. (2023) that the Sagittarius and Perseus spiral arms might merge in the first quadrant before spiraling inward to the far end of the Galactic bar.

Keywords: Interstellar masers (846), Trigonometric parallax (1713), Star forming regions (1565), Milky Way Galaxy (1054)

1. INTRODUCTION

Over the last 16 years, the parallaxes and proper motions of over 200 masers associated with high-mass star-forming regions (HMSFRs) have been measured (Reid et al. 2019, hereafter R19; VERA Collaboration et al. 2020), which trace the spiral arms and three-dimensional (3D) motions of their young stars. While the nearby spiral arms of the Milky Way have been mapped in detail (e.g., Xu et al. 2016), there are few parallax measurements for sources with distances beyond ≈ 10 kpc. In order to extend our mapping of the Milky Way, in this work we report parallax measurements of four distant maser sources, G033.64–00.22, G035.57–00.03, G041.15–00.20, and G043.89–00.78, located past the tangent point of the Sagittarius spiral arm in the first Galactic quadrant. In addition, in order to better constrain the spiral arm structure in distant regions, we also calculate the 3D kinematic distances for several sources whose distances are greater than about 8 kpc. Reid (2022) has shown 3D kinematic distances to be gener-

ally superior to parallax distances for sources well past the Galactic center.

2. OBSERVATIONS AND DATA ANALYSIS

We conducted parallax observations of two 6.7 GHz methanol (CH₃OH) and two 22 GHz water (H₂O) masers over 16 epochs spanning 1.2 yr with the National Radio Astronomy Observatory's (NRAO's)¹ Very Long Baseline Array (VLBA) under program BR210. Prior to our program, G035.57–00.03 had not been observed for a parallax measurement. Parallaxes for the other three sources had been previously published by Wu et al. (2014, 2019). These were specifically chosen for re-observation, because previous parallax measurements (with only 4 or 5 epochs per source) were not

¹ NRAO is a facility of the National Science Foundation operated under cooperative agreement by Associated Universities, Inc.

Table 1. Positions and Brightnesses

Source	R.A. (J2000)	Dec. (J2000)	$\Delta\Theta_E$	$\Delta\Theta_N$	Brightness	V_{LSR}	Beam
	(h m s)	($^{\circ}$ ' ")	($^{\circ}$)	($^{\circ}$)	(Jy/beam)	(km s $^{-1}$)	(mas \times mas @ $^{\circ}$)
G033.64–00.22(M)	18 53 32.56656	+00 31 39.1152	16.0	60.36	6.7×5.1 @ 165
J1848+0138	18 48 21.81041	+01 38 26.6296	–1.3	1.1	0.030		5.1×3.6 @ 173
J1857–0048	18 57 51.35887	–00 48 21.9369	1.1	–1.3	0.053		5.9×3.0 @ 3
G035.57–00.03(W)	18 56 22.52577	+02 20 27.5007	0.9	48.62	1.6×0.5 @ 164
J1855+0251	18 55 35.43649	+02 51 19.5650	–0.2	0.5	0.115		1.4×0.5 @ 164
G041.15–00.20(M)	19 07 14.36746	+07 13 18.0190	3.2	56.00	3.7×1.5 @ 4
J1905+0652	19 05 21.21029	+06 52 10.7830	–0.5	–0.4	0.058		4.2×2.4 @ 6
J1907+0907	19 07 41.96333	+09 07 12.3956	0.1	1.9	0.072		3.9×2.0 @ 179
G043.89–00.78(W)	19 14 26.39610	+09 22 36.5926	8.6	59.18	1.4×0.4 @ 163
J1905+0952	19 05 39.89897	+09 52 08.4075	–2.2	0.5	0.072		1.3×0.6 @ 163
J1913+0932	19 13 24.02535	+09 32 45.3775	–0.3	0.2	0.047		1.5×0.7 @ 159
J1922+0841	19 22 18.63365	+08 41 57.3753	1.9	–0.7	0.013		1.4×0.6 @ 164

NOTE—Source names followed by M and W in parentheses indicate methanol and water masers. $\Delta\Theta_E$ and $\Delta\Theta_N$ are the angular offsets of the QSOs relative to the maser toward the East and North. The absolute position, peak brightness, and (naturally weighted) beam size and position angle (PA; east of north) are listed for the first epoch. Note that the absolute position accuracies are limited to about ± 1 mas from the assumed values for the QSOs. The local standard of rest (LSR) velocities (V_{LSR}) of the reference maser spots are listed for G033.64–00.22, G041.15–00.20, and G043.89–00.78, whereas for G035.57–00.03, J1855+0251 was used as the phase reference.

accurate enough to provide strong constraints on spiral structure for distant portions of the Sagittarius arm.

Details of the observations are listed in Table A1. We scheduled the observations to occur near the extrema of the sinusoidal parallax signatures in R.A., since the parallax amplitudes in decl. were considerably smaller. At each epoch, three 1.7-hr blocks of phase-referenced observations were inserted between four 0.5-hr geodetic blocks, used for clock and atmospheric delay calibrations (see Reid et al. 2009, for details). Four adjacent dual-polarized intermediate-frequency (IF) bands of 16 MHz bandwidth were used for the phase-referenced observations. The maser emissions were centered in the third IF.

The data were correlated in Socorro, New Mexico, with the DiFX² software correlator (Deller et al. 2007). The IF bands containing the masers were correlated with 4000 and 2000 spectral channels for the 6.7 GHz CH₃OH and the 22 GHz H₂O masers, yielding velocity channels of 0.18 and 0.11 km s $^{-1}$, respectively.

We reduced the correlated data with the Astronomical Image Processing System (AIPS; Greisen 2003) and ParseITongue (Kettenis et al. 2006) scripts in four steps as described in Reid et al. (2009). In step 1, we cor-

rected delays and phases for feed rotations, updated Earth’s orientation parameters, ionospheric delays using total electron content maps, residual clock errors, tropospheric delays determined from the geodetic calibration blocks, and updated source positions (when necessary). In step 2, we converted correlator amplitudes to Jansky units by applying telescope gains and system temperatures. In step 3, for the maser data we shifted frequencies to hold LSR velocities at a desired value for all sources and observations. In step 4, one scan on a strong calibrator was chosen to remove delay and phase differences among all bands. In step 5, for all but one source, a channel with strong and compact maser emission was used as the interferometer phase reference and applied to all maser channels and background quasi-stellar objects (QSOs). For G035.57–00.03, the bright background QSO (J1855+0251) was used as the phase reference, because the peak brightness of the H₂O maser (0.9 Jy beam $^{-1}$) provided insufficient signal-to-noise ratios on individual VLBA baselines in 8 kHz spectral channels and 20 s integrations.

The AIPS task IMAGR was used to image the spectral-line emission of the masers and continuum emission of the QSOs. The positions of the maser spots and background QSOs were determined by fitting elliptical Gaussian brightness distributions to the images using the AIPS task JMFIT. Table 1 lists the positions and brightnesses from the first epoch.

² DiFX, a software correlator for very long baseline interferometry (VLBI), is developed as part of the Australian Major National Research Facilities Programme by the Swinburne University of Technology and operated under licence.

Table 2. Astrometric Results

Source	π (mas)	μ_x (mas y ⁻¹)	μ_y (mas y ⁻¹)	V_{LSR} (km s ⁻¹)	D_π (kpc)	D_k (kpc)	D_{ave} (kpc)
G019.60–00.23	0.076 ± 0.011	−3.11 ± 0.16	−6.36 ± 0.17	41 ± 3	13.2 ^{+2.2} _{−1.7}	12.5 ± 0.8	12.6 ± 0.7
G020.08–00.13	0.066 ± 0.010	−3.14 ± 0.14	−6.44 ± 0.16	41 ± 3	15.2 ^{+2.7} _{−2.0}	12.4 ± 0.6	12.7 ± 0.6
G032.74–00.07 [†]	0.126 ± 0.016	−3.15 ± 0.27	−6.10 ± 0.29	37 ± 10	7.9 ^{+1.2} _{−0.9}	11.4 ± 1.0	10.6 ± 0.8
G033.64–00.22 ^{*†‡}	0.103 ± 0.011	−3.01 ± 0.07	−6.30 ± 0.08	^a 61 ± 3	9.7 ^{+1.2} _{−1.0}	10.0 ± 0.6	9.9 ± 0.5
G035.57–00.03 [*]	0.098 ± 0.008	−3.02 ± 0.13	−6.08 ± 0.18	^a 53 ± 3	10.2 ^{+0.9} _{−0.8}	10.2 ± 0.7	10.2 ± 0.6
G035.79–00.17	0.113 ± 0.013	−2.96 ± 0.12	−6.23 ± 0.14	61 ± 5	8.8 ^{+1.2} _{−0.9}	9.6 ± 0.8	9.4 ± 0.6
G037.47–00.10	0.088 ± 0.030	−2.63 ± 0.07	−6.19 ± 0.15	58 ± 3	11.4 ^{+5.9} _{−2.9}	9.4 ± 1.0	9.6 ± 0.9
G038.03–00.30	0.095 ± 0.022	−3.01 ± 0.06	−6.20 ± 0.11	60 ± 3	10.5 ^{+3.2} _{−2.0}	9.2 ± 0.6	9.3 ± 0.6
G041.15–00.20 [†]	0.137 ± 0.011	−2.74 ± 0.15	−6.03 ± 0.16	^b 60 ± 3	7.3 ^{+0.6} _{−0.5}	8.4 ± 1.2	7.6 ± 0.5
G041.22–00.19	0.113 ± 0.022	−2.82 ± 0.13	−5.89 ± 0.16	59 ± 5	8.8 ^{+2.1} _{−1.4}	8.5 ± 1.4	8.7 ± 1.1
G043.03–00.45	0.130 ± 0.019	−3.03 ± 0.15	−6.56 ± 0.20	56 ± 5	7.7 ^{+1.3} _{−1.0}	8.3 ± 0.7	8.2 ± 0.6
G043.89–00.78 ^{*†}	0.136 ± 0.005	−3.01 ± 0.16	−6.03 ± 0.18	^c 54 ± 3	7.3 ^{+0.3} _{−0.3}	8.3 ± 0.8	7.5 ± 0.3
G045.07+00.13	0.129 ± 0.007	−3.21 ± 0.26	−6.11 ± 0.26	59 ± 5	7.8 ^{+0.4} _{−0.4}	7.7 ± 1.0	7.7 ± 0.4
G045.45+00.06	0.119 ± 0.017	−2.34 ± 0.38	−6.00 ± 0.54	55 ± 7	8.4 ^{+1.4} _{−1.1}	7.6 ± 1.4	8.1 ± 0.9
G045.49+00.12	0.144 ± 0.024	−2.62 ± 0.17	−5.61 ± 0.16	58 ± 3	6.9 ^{+1.4} _{−1.0}	7.0 ± 1.6	6.9 ± 0.9
G045.80–00.35	0.137 ± 0.023	−2.52 ± 0.17	−6.08 ± 0.27	64 ± 5	7.3 ^{+1.5} _{−1.0}	6.3 ± 1.5	7.0 ± 1.0

NOTE— Astrometric results are listed for the four sources discussed in this paper and 12 other sources in the Sagittarius arm at distances greater than about 8 kpc. Column 1 lists Galactic source names. Columns 2, 3, and 4 give parallaxes and proper motions in the eastward ($\mu_x = \mu_\alpha \cos \delta$) and northward directions ($\mu_y = \mu_\delta$). Column 5 lists LSR velocities. Columns 6, 7, and 8 list the parallax distances, 3D kinematic distances, and their variance-weighted averages. We adopted these weighted averages in column 8 as the “final” distance. Sources with a superscript (*) are those reported in this paper. Their V_{LSR} are determined from $\text{NH}_3(J, K) = (1, 1)$ emission and the references are (a) Wielen et al. (2012); (b) Pandian et al. (2012); and (c) Olmi et al. (1993). For other sources parallaxes, proper motions, and line-of-sight velocities are taken from Table 1 of R19 (along with their primary references), except for G019.60–00.23 and G020.08–00.13, which are taken from Xu et al. (2021). Sources with a superscript (†) are those having previously published parallaxes, and column 2 lists their weighted averages with the parallax measurements in this paper, as described in Section 3.2. Sources with a superscript (‡) are those flagged as outliers in R19 but included in this paper when determining the characteristics of the Sagittarius arm, as described in Section 4.2.

3. PARALLAX AND DISTANCE ESTIMATES

3.1. Parallax and Proper Motion Fitting

We selected compact maser spots for parallax and proper motion fitting. For the H₂O masers G035.57–00.03 and G043.89–00.78, we first did the parallax and proper motion fitting for each maser spot relative to each background source in order to identify and remove outliers caused by the blending of maser spots. We added “error floors” in the eastern and northern directions in quadrature with the formal positional uncertainties from JMFIT and adjusted them to achieve a reduced χ^2 per degree of freedom near unity in each coordinate. The error floors were used to capture systematic errors in position measurements, usually owing to uncompensated atmospheric delays.

At the lower frequency of the 6.7 GHz methanol maser sources G033.64–00.22 and G041.15–00.20, ionospheric “wedges” can cause systematic positional shifts across the sky, significantly increasing astrometric error. In

order to mitigate this issue, we used an image-position-based method to generate positional data relative to an “artificial quasar” at the target maser position during each epoch. Detailed descriptions of this method can be found in Reid et al. (2017) and Zhang et al. (2019). We adopted this approach (Zhang et al. 2019) in the parallax fits.³

Because all maser spots in a source should have the same parallax, we used all (unblended) maser spots and background sources to carry out a combined solution, which uses a single parallax parameter but allows each maser spot to have a different proper motion. The fitting results for the H₂O and CH₃OH masers are shown in Figures B1 and B2, respectively. Tables B2 and B3 provide detailed results of the parallax and proper motion fits. Since systematic errors caused by propaga-

³ A phase-calibration based procedure, MultiView (Rioja et al. 2017) and inverse MultiView (Hyland et al. 2022), has recently been shown superior to the image-based method, but could not be used with the observing strategy adopted in program BR210.

tion delays are essentially the same for all maser spots, we multiplied the formal parallax uncertainties by the square root of the number of spots used for the parallax fitting (Reid et al. 2009).

Individual fits for G043.89–00.78 with different QSOs revealed some differences among the inferred error-floor values, suggesting different contributions to the systematic error budget from uncompensated atmospheric delays and/or variable unresolved QSO structure. After determining the individual error floors, we added these in quadrature to their formal uncertainties from JMFIT before doing a combined fit. Also, as seen in Figure B1, the decl. data for G043.89–00.78 show the presence of systematics in the residuals, which might be attributed to proper-motion acceleration, possibly owing to orbital acceleration in a long-period stellar binary. Such effects have been seen in Very Long Baseline Interferometric data from Pleiades stars (Melis et al. 2014). When adjustable acceleration parameters were included in the fitting process, these systematic residuals disappeared, as shown by the red dashed line in Figure B1. The estimated acceleration parameters are listed in Table B2. We adopted the parallax results from this approach for G043.89–00.78.

The internal motions of maser features persisting for at least five epochs were averaged to estimate the motion of the central star. Considering typical values of maser spot motions relative to the central star of ~ 5 km s $^{-1}$ (Moscadelli et al. 2002) for 6.7 GHz CH $_3$ OH masers and ~ 10 km s $^{-1}$ (Gwinn et al. 1992) for 22 GHz H $_2$ O masers, for sources with multiple maser features we inflated the formal uncertainties for each proper motion component of the central star by adding ± 3 km s $^{-1}$ and ± 5 km s $^{-1}$ “error floors” in quadrature, respectively. For sources with only one maser feature, we adopted ± 5 km s $^{-1}$ and ± 10 km s $^{-1}$ error floors for the CH $_3$ OH and H $_2$ O masers. We adopted an LSR velocity for the central star based on the centroid of the NH $_3$ molecular line emission (Wienen et al. 2012; Pandian et al. 2012; Olmi et al. 1993).

3.2. Previous Measurements

Regarding G033.64–00.22, Reid et al. (2014) reported a parallax of 0.131 ± 0.020 mas, whereas our data yield a parallax of 0.090 ± 0.014 mas. These two parallaxes are statistically consistent at the 1.7σ level. Combining these two measurements with variance weighting yields a parallax of 0.103 ± 0.011 mas.

For G041.15–00.20, our data yield a parallax of 0.144 ± 0.014 mas, and combining this with the parallax of 0.125 ± 0.018 mas of Wu et al. (2019) yields a variance-weighted average parallax of 0.137 ± 0.011 mas.

For G043.89–00.78, parallaxes of 0.121 ± 0.020 mas and 0.144 ± 0.014 were reported by Wu et al. (2014) and Wu et al. (2019), respectively. Combining these with the our measured parallax of 0.137 ± 0.006 mas yields a parallax of 0.136 ± 0.005 mas.

3.3. 3D Kinematic Distances

The 3D kinematic distances provide an alternative method to estimate distance, independent of parallax measurements. This technique combines likelihoods as a function of distance for line-of-sight velocities and proper motion components in Galactic longitude and latitude, assuming a rotation curve for the Galaxy. Multiplying these three likelihoods yields a posteriori distance estimate, which is generally free of the two-fold ambiguities for standard (1D) kinematic distances using only line-of-sight velocities for sources within the Solar circle (ie, Galactocentric radii less than R_0).

For the four sources discussed in this paper and 12 other sources in the Sagittarius arm whose distances are greater than about 8 kpc, their 3D kinematic distances were estimated using the proper motions, LSR velocities and the Galactic rotation curve of Reid (2022). Table 2 lists their trigonometric parallaxes, proper motions, LSR velocities, the 3D kinematic distances, and a variance-weighted average⁴ of the two distance estimates for each source. We adopted these average distances in the following discussion.

4. DISCUSSION

4.1. Spiral Arm Assignments

We now discuss the spiral arm assignments of the four sources from this paper and the two sources reported by Xu et al. (2021). We assigned maser sources to the spiral arms based on their locations in H I and/or CO longitude–velocity (l, v) diagrams. As shown in Figure 1, traces of the Sagittarius and Perseus arms (Reid et al. 2016) roughly follow the ^{13}CO ($J=1-0$) Galactic Ring Survey (Jackson et al. 2006) integrated from $b = -1^\circ$ to $+1^\circ$. However, for Galactic longitudes lower than about 30° , the near portion of the Sagittarius arm overlaps with the velocities associated with the Perseus arm in (l, v) plots. And, for longitudes less than about 20° , it is difficult to distinguish the far portion of the Sagittarius arm from the Perseus arm. This highlights the need for accurate distance measurements to trace these arms in space.

⁴ We first convert the measured parallax ($\pi \pm \sigma_\pi$) to distance ($d \pm \sigma_d$), where $d = 1/\pi$ and $\sigma_d = d^2\sigma_\pi$, and then combine the parallax-converted distance and the 3D kinematic distance by variance weighting.

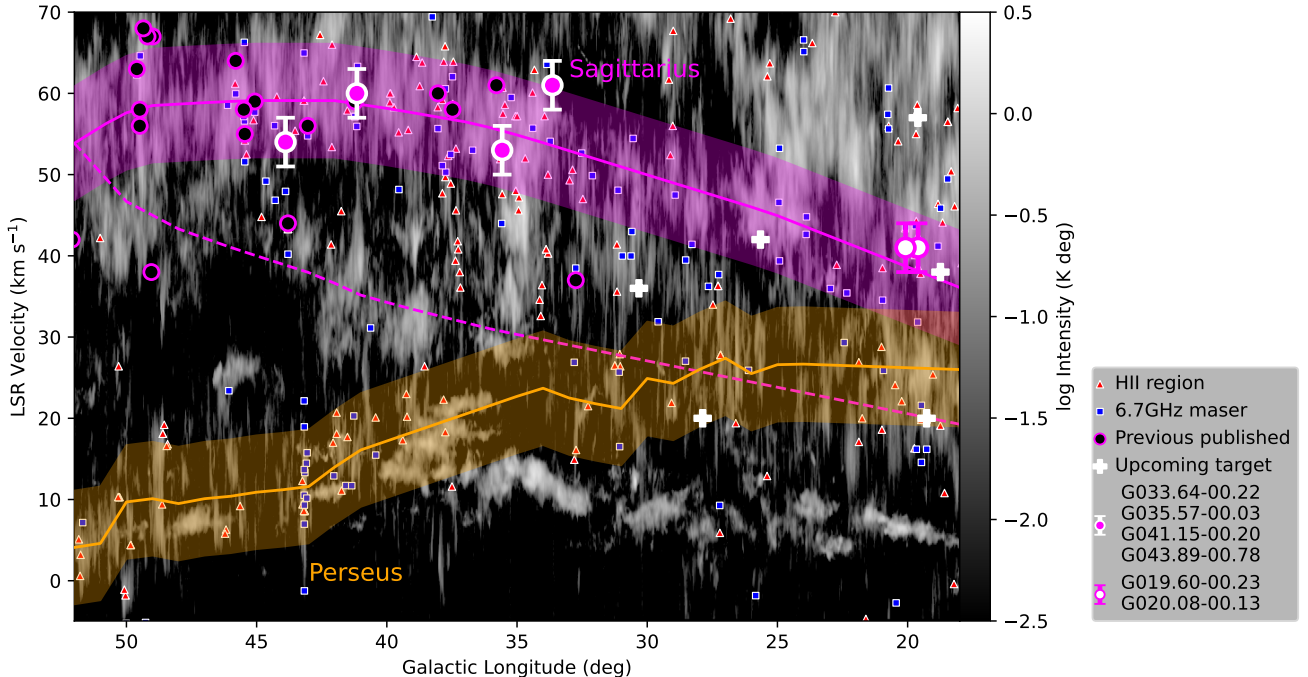


Figure 1. Locations of sources superposed on a CO (l, v) diagram from the Galactic Ring Survey (Jackson et al. 2006) integrated from $b = -1^\circ$ to $+1^\circ$. Black dots with purple edges indicate previously published sources assigned to the far portion of the Sagittarius in the Table 1 of R19 (along with their primary references). White crosses indicate the target for which we are performing VLBA parallax measurements under program BL312 as described in Section 4.2. Red triangles and squares indicate the (l, v) positions of H II regions and 6.7 GHz CH_3OH masers, estimated to be at far kinematic distances in WISE Catalog of Galactic H II Regions (Anderson et al. 2014) and the GLOSTAR Galactic plane survey 6.7 GHz methanol maser catalogue (Nguyen et al. 2022), respectively. Traces of the Sagittarius and Perseus arms from Reid et al. (2016) pass through the CO (Dame et al. 2001; Jackson et al. 2006) and H I (Stil et al. 2006) emission features that define the arms in longitude, latitude, and velocity. The solid and dashed lines correspond to the far and near portions of the Sagittarius arm. The width of the shaded region corresponds to a $\pm 7 \text{ km s}^{-1}$ velocity dispersion.

The (l, v) distribution of H II regions and 6.7 GHz CH_3OH masers, estimated to be at their far kinematic distances in Anderson et al. (2014) and Nguyen et al. (2022), reasonably well follow the Sagittarius and Perseus arms, at least down to Galactic longitudes of about 25° .

As is evident in Figure 1, the (l, v) positions of G033.64–00.22, G035.57–00.03, G041.15–00.20, and G043.89–00.78 indicate unambiguously an association with the far portion of the Sagittarius arm. Figure 2 shows the same four sources (green pentagrams) superposed on a map containing ~ 200 maser sources listed in R19, as well as sources from Xu et al. (2021), and Bian et al. (2022). The locations of our four sources are also consistent with the far portion of the Sagittarius arm. Therefore, we adopt that arm assignment for these four newly measured maser sources.

The distances for G019.60–00.23 and G020.08–00.13 are consistent with either the Sagittarius or Perseus arms. However, the far portion of the Sagittarius arm is favored over the Perseus arm by their (l, v) positions,

since, as shown in Figure 1, their LSR velocities are $\approx 20 \text{ km s}^{-1}$ offset from those expected for the Perseus arm. Typical LSR velocity deviations, owing to internal Virial motions, are $\approx 7 \text{ km s}^{-1}$ from the average arm values (Reid et al. 2016). Also, at longitudes near 20° , the Galactic latitude of the far portion of the Sagittarius arm is $\approx -0^\circ 075$, while that of the Perseus arm is $\approx +0^\circ 076$ (Reid et al. 2016, 2019). At distances of over 12 kpc, the Galactic latitudes of G019.60–00.23 ($-0^\circ 23$) and G020.08–00.13 ($-0^\circ 13$) would place them more than 200 pc below the center of the Perseus arm. Comparing this offset to the (Gaussian 1σ) vertical dispersion of about 100 pc for the Perseus arm (see Fig. 2 of Reid et al. 2016) also favors association with the Sagittarius over the Perseus arm. Considering all the evidence, we confidently assign G019.60–00.23 and G020.08–00.13 to the far portion of the Sagittarius arm.

4.2. Structure of the Sagittarius Arm

R19 fitted log-period spiral functions to the locations of HMSFRs in the Sagittarius arm with trigonometric parallax distances. They found that the Sagittarius arm

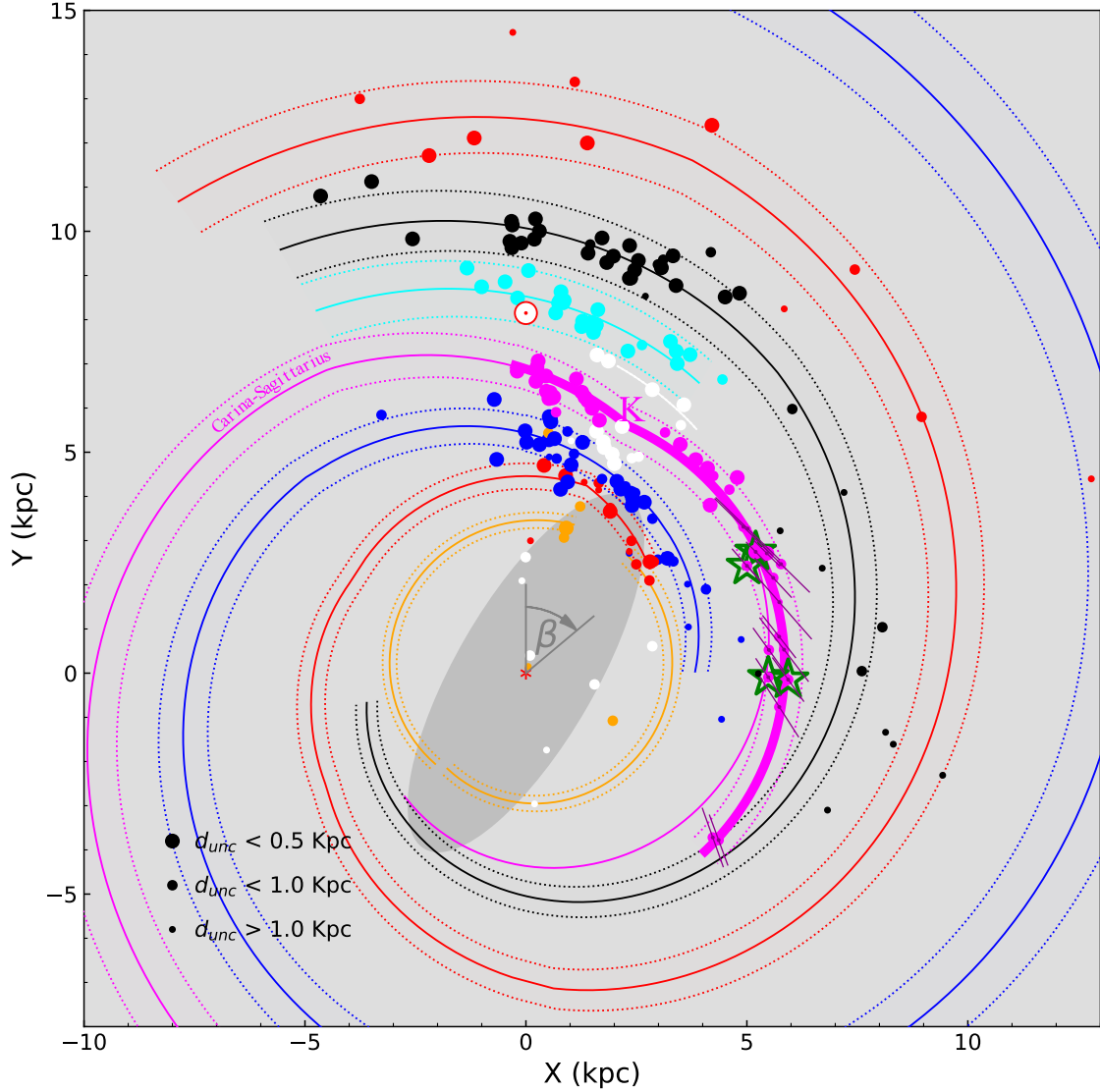


Figure 2. Plan view of the Milky Way as seen from the north Galactic pole following R19. The Galactic center is at (0,0) kpc and the Sun is at (0,8.15) kpc. Solid dots indicate parallax locations of the maser sources. Distance uncertainties are indicated by the inverse size of the symbols as given in the legend at the lower left. Purple dots with 1σ error bars indicate sources described in Section 3 and listed in Table 2. Green stars indicate the locations of the sources reported in this paper. The spiral arm models from R19 are traced with solid lines and dotted lines enclose 90% of the sources. The location of the kink in Sagittarius arm is marked with a "K." The long Galactic bar is indicated with a shaded ellipse (Wegg et al. 2015). The pitch angle fit for the Sagittarius arm determined in this paper is traced with a thick purple line.

has a “kink” at Galactocentric azimuth $\beta \approx 24^\circ$ with pitch angles of $17^\circ.1 \pm 1^\circ.6$ for $2^\circ < \beta < 24^\circ$, and $1^\circ.0 \pm 2^\circ.1$ for $24^\circ < \beta < 97^\circ$. Beyond the Galactic center (i.e., $\beta > 90^\circ$), only two sources, G037.47–00.10 and G038.03–00.30, with parallaxes reported by Wu et al. (2019), were used by R19 to characterize the Sagittarius arm. Our results for G033.64–00.22 and G035.57–00.03 together with the measurements of G019.60–00.23 and G020.08–00.13 (Xu et al. 2021) add significant weight in determining the arm structure in this distant region. Using these six distant sources, adopting the averaged

distances given in Table 2, and the same methodology as R19, we redetermine the characteristics of the Sagittarius arm over an extended range. It is worth noting that, while employing the same procedure as R19, the increased accuracy of distances in Table 2 has resulted in two R19 outliers (G032.74–00.07 and G033.64–00.22, with $> 3\sigma$ residuals), now being within the acceptable range ($< 3\sigma$ residuals).

We estimate the pitch angles of the two Sagittarius arm segments to be $18^\circ.6 \pm 1^\circ.4$ and $1^\circ.5 \pm 1^\circ.1$ for segments between azimuths of $-2^\circ < \beta < 22^\circ$ and

$22^\circ < \beta < 132^\circ$, respectively. Our best-fitting parameters are consistent with the results of R19 (17.1 ± 1.6 and 1.0 ± 2.1 for the segments between azimuths of $2^\circ < \beta < 24^\circ$ and $24^\circ < \beta < 97^\circ$, respectively). Our results, based on more parallax data, extend the azimuth range from 97° to 132° (see Table 3). In addition, the significant decrease in the uncertainty of the pitch angle for $\beta > 22^\circ$ between the estimate of R19 and ours suggests that the pitch angle is nearly constant over the azimuth range $22^\circ < \beta < 132^\circ$. We plot our extended model as the thick purple line in Figure 2.

While our fitted pitch angles are close to those of R19, our model for the Sagittarius arm in Fig. 2 starting near $\beta = 42^\circ$ traces radially outward from the R19 model, and by $\beta = 132^\circ$ it is at ≈ 1 kpc greater radius. Why does this occur? When the R19 model was generated, G019.60–00.23 and G020.08–00.13 had not yet been measured, and G032.74–00.07 and G033.64–00.22 were flagged as outliers (and not used in their arm fitting). Thus, the pitch angle for $\beta > 42^\circ$ was not well constrained. In order to build a more complete spiral arm model for the Milky Way, for the distant portion of the Sagittarius arm they adopted a pitch angle of 8° , which was closer to the average value determined for the spiral arms in the Milky Way and extrapolated the Sagittarius arm to the far end of the Galactic bar at approximately the same radius as that measured for the Norma arm at the near end of the bar.

As seen in Figure 2, our updated model for the far portion of the Sagittarius arm, based on new parallax and 3D kinematic distance measurements, approaches the R19 model for the Perseus arm at $\beta \approx 130^\circ$. This supports the suggestion (Xu et al. 2023) that the Sagittarius and Perseus arm might merge. However, we note that the location of the Perseus arm for azimuths greater than $\approx 90^\circ$ is currently not well constrained, and the Perseus and Sagittarius arms might merge closer to the far end of the bar, or they may not merge at all.

As can be seen in the shaded regions of Figure 1, there are dozens of 6.7 GHz masers at $\ell \approx 20^\circ$ to 35° that could be associated with the far portion of the Sagittarius arm or Perseus arms. Parallax measurements for these sources using the MultiView calibration technique (Rioja et al. 2017; Hyland et al. 2022) could help us to test these possibilities. In fact, for this purpose, under program BL312 (from March 2024 to March 2025), we are measuring the parallax of eight maser sources. Six of the eight sources are in the scope of Figure 1, shown as white crosses.

4.3. Kinematics of the Sagittarius Arm

The peculiar motion components, U_s (toward the Galactic center), V_s (in the direction of Galactic rotation), and W_s (toward the north Galactic pole) listed in Table C4 for the maser sources listed in Table 2 were calculated by adopting the distance to the Galactic center, $R_0 = 8.15$ kpc; the circular rotation speed at the Sun, $\Theta_0 = 236$ km s $^{-1}$ the solar motion values $U_\odot = 10.6$ km s $^{-1}$, $V_\odot = 10.7$ km s $^{-1}$, and $W_\odot = 7.6$ km s $^{-1}$; and the Galactic rotation curve from R19.

Figure 3 shows the peculiar motions components (U_s , V_s , W_s) as a function of Galactic azimuth (β) for sources in the Sagittarius arm based on the data from this paper and Table 1 of R19. From Figure 3, one can see that all values are consistent with 0 ± 20 km s $^{-1}$. The variance-weighted average peculiar motion components ($\overline{U_s}$, $\overline{V_s}$, $\overline{W_s}$) for the Sagittarius arm sources are listed in Table 4. For comparison with other spiral arms, the corresponding values for the sources in the Norma, Scutum, Local, Perseus, and Outer arms are also listed in Table 4 (based on data in Table 1 of R19). Among these spiral arms, the Sagittarius arm has the among the smallest $\overline{U_s}$ and $\overline{V_s}$ magnitudes, indicating near circular Galactic orbits. However, the Sagittarius arm has the only statistically significant $\overline{W_s}$ value, which comes from sources in the arm segment with $\beta < 22^\circ$ mostly moving toward the South Galactic Pole.

5. SUMMARY

We measured the parallaxes and proper motions of four masers in HMSFRs associated with the distant portions of the Sagittarius spiral arm. The results for G041.15–00.20 and G043.89–00.78 at Galactic azimuth $\beta \sim 80^\circ$ are consistent with the previous model for the arm by R19. However, the more distant sources, G033.64–00.22 and G035.57–00.03, as well as G019.60–00.23 and G020.08–00.13 from Xu et al. (2021), better constrain the structure of the Sagittarius arm beyond the Galactic center ($\beta > 90^\circ$) and suggest that the Sagittarius arm model of R19 should be moved outward by about 1 kpc at $\beta \approx 130^\circ$, where it might merge with the Perseus arm.

- 1 This work was funded by the National SKA Program
- 2 of China (grant No. 2022SKA0120103), NSFC grant
- 3 11933011, 12303072, the Key Laboratory for Radio As-
- 4 tronomy, the Jiangsu Funding Program for Excellent
- 5 Postdoctoral Talent (grant No. 2023ZB093), and the
- 6 Natural Science Foundation of Jiangsu Province (grant
- 7 No. BK20210999).

Table 3. Sagittarius Arm Fitting Results

Reference	l Tangency	β Range	β_{kink}	R_{kink}	$\psi_{<}$	$\psi_{>}$	Width
	(deg)	(deg)	(deg)	(kpc)	(deg)	(deg)	(kpc)
This paper	284.4	$-2 \rightarrow 132$	22 ± 2	6.06 ± 0.06	18.4 ± 1.4	1.7 ± 1.0	0.18 ± 0.03
R19	285.6	$2 \rightarrow 97$	24 ± 2	6.04 ± 0.09	17.1 ± 1.6	1.0 ± 2.1	0.27 ± 0.04

NOTE—Parameters estimated from fitting log-periodic spirals to the Sagittarius arm based on data from this paper, Xu et al. (2021), and R19, assuming the distance to the Galactic center of $R_0 = 8.15$ kpc. An arm tangency prior of $283 \pm 2^\circ$ (Bronfman et al. 2000) was used to constrain the fit. Column 2 lists the fitted tangency. Column 3 lists the azimuth range of the parallax data. Columns 4 and 5 list the Galactic azimuth and radius of the arm kink, separating two arm segments. Columns 6 and 7 give pitch angles for azimuths less and greater than β_{kink} . Column 9 lists the intrinsic (Gaussian 1σ) arm width at R_{kink} . Rows 1 and 2 give the best-fitting parameters in this paper and from R19 for comparison.

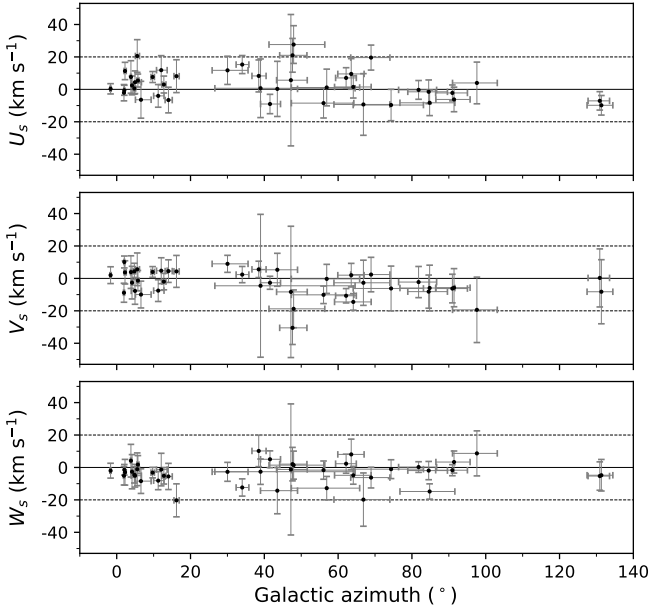


Figure 3. Plots of the peculiar motion components vs. Galactic azimuth for sources in the Sagittarius arm based on the data from this paper and Table 1 of R19. The top, middle, and bottom panels show U_s , V_s , and W_s , respectively, calculated by adopting model A5 and the Galactic rotation curve from R19.

Facility: VLBA

Table 4. Average Peculiar Motions of HMSFRs in Spiral Arms

Arm	N	\overline{U}_s	\overline{V}_s	\overline{W}_s
Name		(km s $^{-1}$)	(km s $^{-1}$)	(km s $^{-1}$)
Norma	14	9.9 ± 3.2	-7.7 ± 1.7	0.2 ± 1.7
Scutum	40	10.8 ± 1.3	-1.4 ± 1.1	-0.7 ± 1.0
Sagittarius	42	2.2 ± 1.0	-0.8 ± 1.0	-3.0 ± 0.9
Local	28	0.1 ± 1.0	-7.4 ± 0.9	1.7 ± 1.0
Perseus	41	8.7 ± 0.9	-5.9 ± 1.1	0.1 ± 1.0
Outer	11	5.7 ± 1.9	-6.7 ± 2.6	0.7 ± 2.4

NOTE—Variance-weighted averages of peculiar motions were calculated from data in this paper and Table 1 of R19. Columns 1 and 2 list the arm name and the number of sources. Columns 3, 4, and 5 list the variance-weighted average of the peculiar motion components U_s , V_s , and W_s .

Table A1. Dates of VLBA Observations

G033.64–00.22	G035.57–00.03	G041.15–00.20	G043.89–00.78
2015 Mar 01	2015 Mar 08	2015 Mar 01	2015 Mar 08
2015 Mar 28	2015 Mar 27	2015 Mar 28	2015 Mar 27
2015 Apr 22	2015 Apr 20	2015 Apr 22	2015 Apr 20
2015 May 20	2015 May 14	2015 May 20	2015 May 14
2015 Aug 28	2015 Aug 29	2015 Aug 28	2015 Aug 29
2015 Sep 10	2015 Sep 13	2015 Sep 10	2015 Sep 13
2015 Sep 21	2015 Sep 28	2015 Sep 21	2015 Sep 28
2015 Oct 03	2015 Oct 09	2015 Oct 03	2015 Oct 09
2015 Oct 16	2015 Oct 24	2015 Oct 16	2015 Oct 24
2015 Oct 27	2015 Nov 02	2015 Oct 27	2015 Nov 02
2015 Nov 06	2015 Nov 13	2015 Nov 06	2015 Nov 13
2015 Nov 16	2015 Nov 23	2015 Nov 16	2015 Nov 23
2016 Feb 26	2016 Feb 25	2016 Feb 26	2016 Feb 25
2016 Mar 25	2016 Mar 22	2016 Mar 25	2016 Mar 22
2016 Apr 18	2016 Apr 16	2016 Apr 18	2016 Apr 16
2016 May 26	2016 May 25	2016 May 26	2016 May 25

APPENDIX

A. OBSERVATIONS

Here, we list the details of the epochs observed in Table A1.

B. PARALLAX AND PROPER MOTION FITS

Here, we list the details of the parallaxes fits with formal uncertainties and the proper motion estimations listed in Table B2 and Table B3, respectively.

C. PECULIAR MOTIONS

Here, we list the peculiar motions of the sources located in the Sagittarius arm in Table C4.

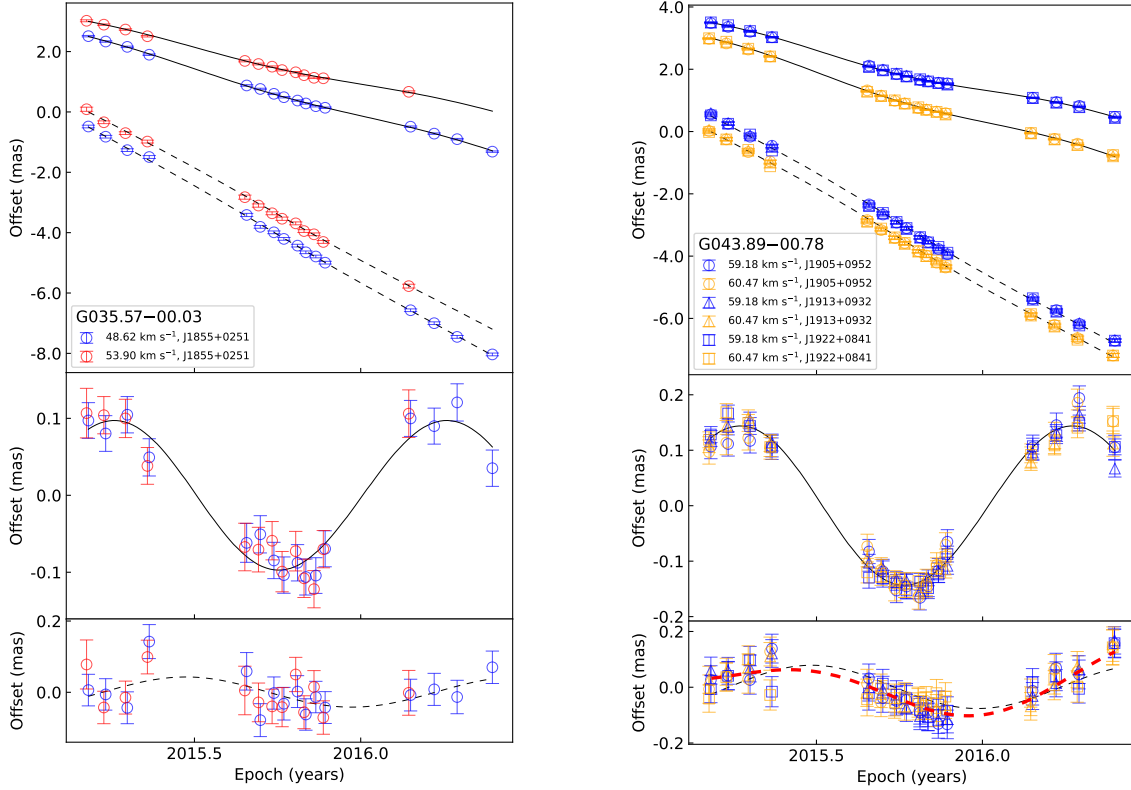


Figure B1. Parallax fitting results for the H₂O masers G035.57–00.03 and G043.89–00.78. The top panels give the eastward (solid line) and northward (dashed line) position offsets vs. time. The middle and bottom panels display the eastward and northward data with the fitted proper motion removed. See the legend for the source names, the V_{LSR} of each maser spot, and the background QSO(s) used for the position reference(s). The red dashed line shows the northward position offsets when proper-motion acceleration was included in the fitting process for G043.89–00.78.

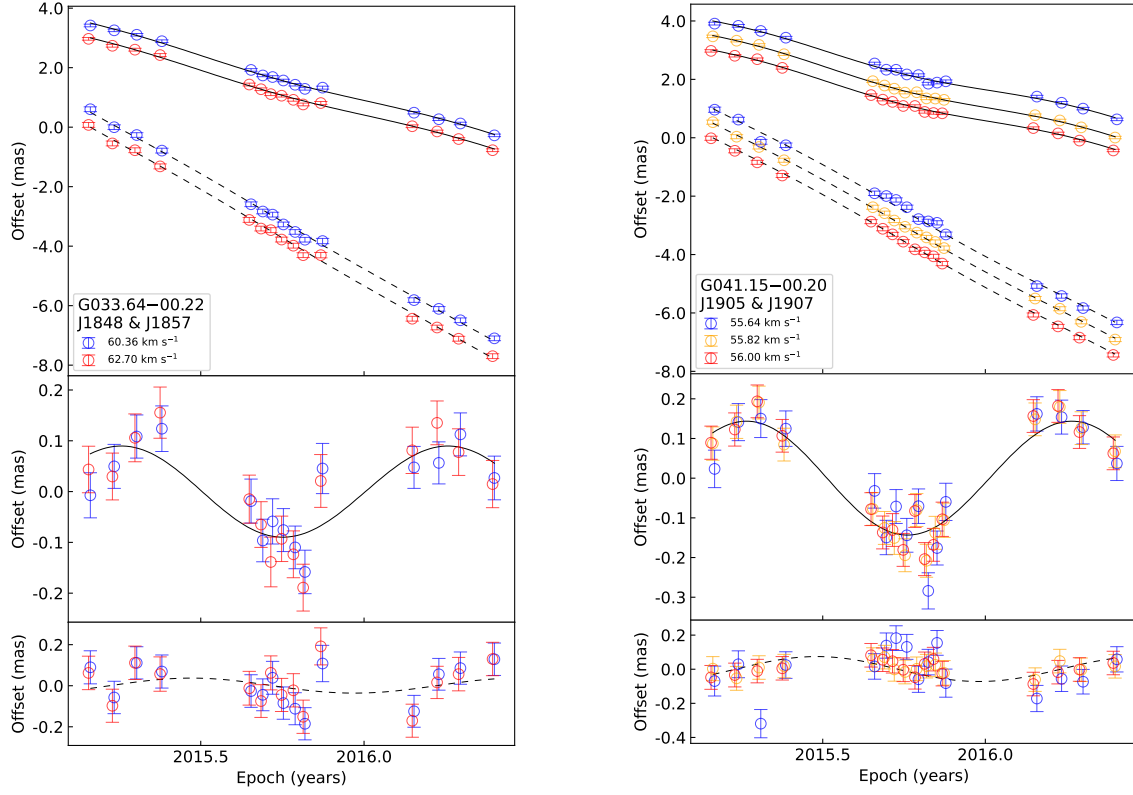


Figure B2. Same as Figure B1, but for the CH₃OH masers, G033.64-00.22 and G041.15-00.20. Their parallaxes are estimated using the approach of Zhang et al. (2019).

Table B2. Detailed Results of the Parallaxes

Target	Background	V_{LSR}	Detected	Parallax	Solved for	acc_x	acc_y	
Source	Source	(km s^{-1})	epochs	(mas)	acceleration	(mas y^{-2})	(mas y^{-2})	
H ₂ O maser								
G035.57–00.03	J1855+0251	48.62	1111 1111 1111 1111	0.098 ± 0.006	No			
		53.90	1111 1111 1111 1000	0.098 ± 0.013	No			
	Combined fit			0.098 ± 0.008	No			
G043.89–00.78	J1905+0952	59.18	1111 11111111 1111	0.146 ± 0.006	No			
		60.47	1111 11111111 1111	0.142 ± 0.006	No			
	J1913+0932	59.18	1111 11111111 1111	0.143 ± 0.004	No			
		60.47	1111 11111111 1111	0.140 ± 0.004	No			
	J1922+0841	59.18	1111 11111111 1111	0.150 ± 0.003	No			
		60.47	1111 11111111 1111	0.145 ± 0.005	No			
		Combined fit			0.145 ± 0.003	No		
	G043.89–00.78	J1905+0952	59.18	1111 11111111 1111	0.153 ± 0.012	Yes	-0.12 ± 0.16	0.62 ± 0.12
60.47			1111 11111111 1111	0.129 ± 0.013	Yes	0.16 ± 0.18	0.48 ± 0.12	
J1913+0932		59.18	1111 11111111 1111	0.157 ± 0.007	Yes	-0.21 ± 0.09	0.73 ± 0.05	
		60.47	1111 11111111 1111	0.130 ± 0.009	Yes	0.11 ± 0.13	0.55 ± 0.09	
J1922+0841		59.18	1111 11111111 1111	0.140 ± 0.007	Yes	0.11 ± 0.09	0.43 ± 0.15	
		60.47	1111 11111111 1111	0.119 ± 0.010	Yes	0.36 ± 0.14	0.26 ± 0.16	
		Combined fit			0.137 ± 0.006	Yes	0.08 ± 0.06	0.54 ± 0.05
CH ₃ OH maser								
G033.64–00.22	J848 & J1857	60.36	1111 1111 1101 1111	0.081 ± 0.018	No			
		62.70	1111 1111 1101 1111	0.099 ± 0.019	No			
	Combined fit			0.090 ± 0.014	No			
G041.15–00.20	J1905 & J1907	55.64	1111 1111 1111 1111	0.128 ± 0.026	No			
		55.82	1111 1111 1111 1111	0.140 ± 0.016	No			
		56.00	1111 1111 1111 1111	0.141 ± 0.015	No			
	Combined fit			0.144 ± 0.014	No			

Table B3. Detailed Results of the Proper Motions

Target	Feature	V_{LSR}	μ_x	μ_y	Δx	Δy
Source		(km s ⁻¹)	(mas y ⁻¹)	(mas y ⁻¹)	(mas)	(mas)
H ₂ O maser						
G035.57–00.03	1	48.19~49.05	-3.11 ± 0.04	-6.26 ± 0.07	0	0
	2	64.50~68.71	-3.23 ± 0.11	-6.02 ± 0.21	624	-1088
	3	55.75~56.07	-3.17 ± 0.07	-6.16 ± 0.17	-319	-303
	4	50.56~54.88	-2.45 ± 0.06	-5.93 ± 0.11	53	46
	5	53.16~53.59	-3.16 ± 0.12	-6.04 ± 0.20	1428	596
	Average		-3.02 ± 0.08	-6.08 ± 0.15		
	Enlarge 5 km s ⁻¹ Error		-3.02 ± 0.13	-6.08 ± 0.18		
G043.89–00.78	1	58.10~59.61	-2.48 ± 0.03	-6.08 ± 0.03	0	0
	2	48.71~51.73	-3.42 ± 0.04	-5.02 ± 0.05	-62	-51
	3	59.72~60.80	-3.09 ± 0.03	-5.81 ± 0.13	-78	-102
	4	54.43~56.37	-3.03 ± 0.10	-7.22 ± 0.14	-65	-276
		Average		-3.01 ± 0.05	-6.03 ± 0.09	
	Enlarge 5 km s ⁻¹ Error		-3.01 ± 0.16	-6.03 ± 0.18		
CH ₃ OH maser						
G033.64–00.22	1	60.18~60.54	-3.01 ± 0.03	-6.26 ± 0.05	0	0
	2	62.52~63.24	-3.00 ± 0.04	-6.33 ± 0.06	-28	-2
		Average		-3.01 ± 0.04	-6.30 ± 0.06	
	Enlarge 3 km s ⁻¹ Error		-3.01 ± 0.07	-6.30 ± 0.08		
G041.15–00.20	1	55.65~56.00	-2.74 ± 0.03	-6.03 ± 0.06	0	0
		Enlarge 5 km s ⁻¹ Error		-2.74 ± 0.15	-6.03 ± 0.16	

Table C4. Peculiar Motions

Source	β	U_s	V_s	W_s	Distance	μ_x	μ_y	v_{LSR}
	(°)	(km s ⁻¹)	(km s ⁻¹)	(km s ⁻¹)	kpc	mas y ⁻¹	mas y ⁻¹	km s ⁻¹
G045.49+00.12	56.0 ^{+8.2} _{-8.7}	-8.5 ± 9.2	-10.1 ± 5.4	-1.6 ± 5.6	6.9 ^{+0.9} _{-0.9}	-2.62 ± 0.17	-5.61 ± 0.16	58 ± 3
G045.80–00.35	56.9 ^{+8.9} _{-9.6}	1.1 ± 11.3	-0.3 ± 9.0	-12.8 ± 7.2	7.0 ^{+1.0} _{-1.0}	-2.52 ± 0.17	-6.08 ± 0.27	64 ± 5
G043.89–00.78	62.2 ^{+2.8} _{-2.8}	7.0 ± 6.3	-10.7 ± 4.4	2.3 ± 5.9	7.5 ^{+0.3} _{-0.3}	-3.01 ± 0.16	-6.03 ± 0.18	54 ± 3
G045.07+00.13	63.6 ^{+3.5} _{-3.6}	9.5 ± 9.4	2.0 ± 7.3	8.1 ± 9.4	7.7 ^{+0.4} _{-0.4}	-3.21 ± 0.26	-6.11 ± 0.26	59 ± 5
G041.15–00.20	64.1 ^{+4.8} _{-5.1}	1.5 ± 6.8	-14.5 ± 5.1	-4.9 ± 5.5	7.6 ^{+0.5} _{-0.5}	-2.74 ± 0.15	-6.03 ± 0.16	60 ± 3
G045.45+00.06	66.9 ^{+7.2} _{-8.0}	-9.3 ± 19.0	-2.7 ± 13.9	-19.8 ± 16.4	8.1 ^{+0.9} _{-0.9}	-2.34 ± 0.38	-6.00 ± 0.54	55 ± 7
G043.03–00.45	68.9 ^{+5.1} _{-5.5}	19.6 ± 7.7	2.4 ± 10.6	-6.2 ± 6.4	8.2 ^{+0.6} _{-0.6}	-3.03 ± 0.15	-6.56 ± 0.20	56 ± 5
G041.22–00.19	74.3 ^{+8.8} _{-10.3}	-9.7 ± 9.7	-6.2 ± 13.8	-1.1 ± 5.8	8.7 ^{+1.1} _{-1.1}	-2.82 ± 0.13	-5.89 ± 0.16	59 ± 5
G038.03–00.30	81.8 ^{+4.9} _{-5.4}	-0.3 ± 5.8	-2.3 ± 9.6	0.2 ± 3.3	9.3 ^{+0.6} _{-0.6}	-3.01 ± 0.06	-6.20 ± 0.11	60 ± 3
G035.79–00.17	84.5 ^{+5.1} _{-5.7}	-1.5 ± 7.3	-8.2 ± 10.2	-1.9 ± 5.6	9.4 ^{+0.6} _{-0.6}	-2.96 ± 0.12	-6.23 ± 0.14	61 ± 5
G037.47–00.10	84.8 ^{+6.8} _{-8.0}	-8.3 ± 7.9	-5.9 ± 14.1	-14.8 ± 4.7	9.6 ^{+0.9} _{-0.9}	-2.63 ± 0.07	-6.19 ± 0.15	58 ± 3
G033.64–00.22	91.0 ^{+4.1} _{-4.5}	-2.2 ± 4.9	-6.3 ± 8.8	-1.7 ± 3.4	9.9 ^{+0.5} _{-0.5}	-3.01 ± 0.07	-6.30 ± 0.08	61 ± 3
G035.57–00.03	91.4 ^{+4.4} _{-4.9}	-6.2 ± 7.6	-5.7 ± 11.8	3.3 ± 6.8	10.2 ^{+0.6} _{-0.6}	-3.02 ± 0.13	-6.08 ± 0.18	53 ± 3
G032.74–00.07	97.6 ^{+5.5} _{-6.6}	3.9 ± 12.9	-19.4 ± 20.2	8.7 ± 13.9	10.6 ^{+0.8} _{-0.8}	-3.15 ± 0.27	-6.10 ± 0.29	37 ± 10
G020.08–00.13	130.9 ^{+2.6} _{-3.2}	-7.1 ± 5.7	0.3 ± 17.9	-5.3 ± 8.7	12.7 ^{+0.6} _{-0.6}	-3.14 ± 0.14	-6.44 ± 0.16	41 ± 3
G019.60–00.23	131.3 ^{+3.1} _{-3.9}	-9.8 ± 6.0	-8.2 ± 19.8	-4.8 ± 9.7	12.6 ^{+0.7} _{-0.7}	-3.11 ± 0.16	-6.36 ± 0.17	41 ± 3

NOTE—Peculiar motion for sources listed in Table 2. Column 1 lists the source names nominated with Galactic coordinates. The sources are sorted in increasing Galactic azimuth as listed in Column 2. Columns 3, 4, and 5 list the peculiar motions toward the Galactic center, in the direction of Galactic rotation, and toward the north Galactic pole, respectively. Columns 6–9 list the distances, proper motions in the eastward and northward directions, and LSR velocities, respectively. The Galactic “Univ” model and solar motions found by R19 were used to calculate the peculiar motions.

REFERENCES

- Anderson, L. D., Bania, T. M., Bailer, D. S., et al. 2014, *ApJS*, 212, 1, doi: [10.1088/0067-0049/212/1/1](https://doi.org/10.1088/0067-0049/212/1/1)
- Bian, S. B., Xu, Y., Li, J. J., et al. 2022, *AJ*, 163, 54, doi: [10.3847/1538-3881/ac3d90](https://doi.org/10.3847/1538-3881/ac3d90)
- Bronfman, L., Casassus, S., May, J., & Nyman, L. Å. 2000, *A&A*, 358, 521, doi: [10.48550/arXiv.astro-ph/0006104](https://doi.org/10.48550/arXiv.astro-ph/0006104)
- Dame, T. M., Hartmann, D., & Thaddeus, P. 2001, *ApJ*, 547, 792, doi: [10.1086/318388](https://doi.org/10.1086/318388)
- Deller, A. T., Tingay, S. J., Bailes, M., & West, C. 2007, *PASP*, 119, 318, doi: [10.1086/513572](https://doi.org/10.1086/513572)
- Greisen, E. W. 2003, in *Astrophysics and Space Science Library*, Vol. 285, *Information Handling in Astronomy - Historical Vistas*, ed. A. Heck, 109, doi: [10.1007/0-306-48080-8_7](https://doi.org/10.1007/0-306-48080-8_7)
- Gwinn, C. R., Moran, J. M., & Reid, M. J. 1992, *ApJ*, 393, 149, doi: [10.1086/171493](https://doi.org/10.1086/171493)
- Hyland, L. J., Reid, M. J., Ellingsen, S. P., et al. 2022, *ApJ*, 932, 52, doi: [10.3847/1538-4357/ac6d5b](https://doi.org/10.3847/1538-4357/ac6d5b)
- Jackson, J. M., Rathborne, J. M., Shah, R. Y., et al. 2006, *ApJS*, 163, 145, doi: [10.1086/500091](https://doi.org/10.1086/500091)
- Kettenis, M., van Langevelde, H. J., Reynolds, C., & Cotton, B. 2006, in *Astronomical Society of the Pacific Conference Series*, Vol. 351, *Astronomical Data Analysis Software and Systems XV*, ed. C. Gabriel, C. Arviset, D. Ponz, & S. Enrique, 497
- Melis, C., Reid, M. J., Mioduszewski, A. J., Stauffer, J. R., & Bower, G. C. 2014, *Science*, 345, 1029, doi: [10.1126/science.1256101](https://doi.org/10.1126/science.1256101)
- Moscadelli, L., Menten, K. M., Walmsley, C. M., & Reid, M. J. 2002, *ApJ*, 564, 813, doi: [10.1086/324304](https://doi.org/10.1086/324304)
- Nguyen, H., Rugel, M. R., Murugesan, C., et al. 2022, *A&A*, 666, A59, doi: [10.1051/0004-6361/202244115](https://doi.org/10.1051/0004-6361/202244115)
- Olmi, L., Cesaroni, R., & Walmsley, C. M. 1993, *A&A*, 276, 489
- Pandian, J. D., Wyrowski, F., & Menten, K. M. 2012, *ApJ*, 753, 50, doi: [10.1088/0004-637X/753/1/50](https://doi.org/10.1088/0004-637X/753/1/50)
- Reid, M. J. 2022, *AJ*, 164, 133, doi: [10.3847/1538-3881/ac80bb](https://doi.org/10.3847/1538-3881/ac80bb)
- Reid, M. J., Dame, T. M., Menten, K. M., & Brunthaler, A. 2016, *ApJ*, 823, 77, doi: [10.3847/0004-637X/823/2/77](https://doi.org/10.3847/0004-637X/823/2/77)
- Reid, M. J., Menten, K. M., Brunthaler, A., et al. 2009, *ApJ*, 693, 397, doi: [10.1088/0004-637X/693/1/397](https://doi.org/10.1088/0004-637X/693/1/397)
- . 2014, *ApJ*, 783, 130, doi: [10.1088/0004-637X/783/2/130](https://doi.org/10.1088/0004-637X/783/2/130)
- Reid, M. J., Brunthaler, A., Menten, K. M., et al. 2017, *AJ*, 154, 63, doi: [10.3847/1538-3881/aa7850](https://doi.org/10.3847/1538-3881/aa7850)
- Reid, M. J., Menten, K. M., Brunthaler, A., et al. 2019, *ApJ*, 885, 131, doi: [10.3847/1538-4357/ab4a11](https://doi.org/10.3847/1538-4357/ab4a11)
- Rioja, M. J., Dodson, R., Orosz, G., Imai, H., & Frey, S. 2017, *AJ*, 153, 105, doi: [10.3847/1538-3881/153/3/105](https://doi.org/10.3847/1538-3881/153/3/105)
- Stil, J. M., Taylor, A. R., Dickey, J. M., et al. 2006, *AJ*, 132, 1158, doi: [10.1086/505940](https://doi.org/10.1086/505940)
- VERA Collaboration, Hirota, T., Nagayama, T., et al. 2020, *PASJ*, 72, 50, doi: [10.1093/pasj/psaa018](https://doi.org/10.1093/pasj/psaa018)
- Wegg, C., Gerhard, O., & Portail, M. 2015, *MNRAS*, 450, 4050, doi: [10.1093/mnras/stv745](https://doi.org/10.1093/mnras/stv745)
- Wienen, M., Wyrowski, F., Schuller, F., et al. 2012, *A&A*, 544, A146, doi: [10.1051/0004-6361/201118107](https://doi.org/10.1051/0004-6361/201118107)
- Wu, Y. W., Sato, M., Reid, M. J., et al. 2014, *A&A*, 566, A17, doi: [10.1051/0004-6361/201322765](https://doi.org/10.1051/0004-6361/201322765)
- Wu, Y. W., Reid, M. J., Sakai, N., et al. 2019, *ApJ*, 874, 94, doi: [10.3847/1538-4357/ab001a](https://doi.org/10.3847/1538-4357/ab001a)
- Xu, Y., Hao, C. J., Liu, D. J., et al. 2023, *ApJ*, 947, 54, doi: [10.3847/1538-4357/acc45c](https://doi.org/10.3847/1538-4357/acc45c)
- Xu, Y., Reid, M., Dame, T., et al. 2016, *Science Advances*, 2, e1600878, doi: [10.1126/sciadv.1600878](https://doi.org/10.1126/sciadv.1600878)
- Xu, Y., Bian, S. B., Reid, M. J., et al. 2021, *ApJS*, 253, 1, doi: [10.3847/1538-4365/abd8cf](https://doi.org/10.3847/1538-4365/abd8cf)
- Zhang, B., Reid, M. J., Zhang, L., et al. 2019, *AJ*, 157, 200, doi: [10.3847/1538-3881/ab141d](https://doi.org/10.3847/1538-3881/ab141d)